ADVANCED ELECTRONIC MATERIALS Open Access
www.advelectronicmat.de

Phase-Coherent Transport in GeSn Alloys on Si

Prateek Kaul, Omar Concepción, Daan H. Wielens, Patrick Zellekens, Chuan Li, Zoran Ikonic, Koji Ishibashi, Qing-Tai Zhao, Alexander Brinkman, Detlev Grützmacher, and Dan Buca**

Germanium-Tin (GeSn) is a novel semiconductor Group IV alloy that can be tuned from indirect to direct bandgap semiconductors by adjusting the Sn content. This property makes this alloy class attractive for integrated photonic applications and high-mobility electronic devices. In this work, the GeSn alloy properties are investigated in the view of applications fields such as spintronics and quantum computing. Using low-temperature magneto-transport measurements, electron interference effects and deriving typical mesoscopic benchmark parameters such as the phase-coherence length in GeSn-based Hall bar structures for Sn concentrations up to 14 at.% is investigated. Furthermore, Shubnikov–de Haas oscillations provide direct access to the effective mass of the Γ-valley electrons as well as the charge carrier mobility. This work provides a new insight into advanced group IV alloys desired for the study of spin dynamics and its quantum computing applications.

1. Introduction

Ever since the idea of spin manipulation for quantum computing was conceived,[1] significant research has been implemented to control the spins of electrons and holes in semiconductors, along with the exploration of new physics in the spintronics field.[2,3] Spin manipulation and control offer a solution for the present-day Moore's law problem of increased power dissipation in electronic circuits while scaling down the technology and improving the performance.[4] Initial works in this field were based on electron spins in III–V heterostructures, but the strong nuclear spins and the hyperfine interaction with the nuclear spins are the main factors affecting the electron spin coherence time.[5] In group-IV semiconductors, such as silicon, isotopic purification offers a very long electron coherence length.[6,7] Furthermore, Si is the natural platform for the co-integration of quantum devices with classical driving electronics, also compatible with the scalability of the established Si complementary metal-oxide-semiconductor (CMOS) technology.[8] Beyond electrons, holes are the next promising step due to their high spin-orbit coupling (SOC) which allows to electrical control of the spins by the Rashba effect, eliminating the need for local micro-magnets like in the Si platform.[9] Therefore, germanium (Ge) is a promising material for hole-based spin-qubits due to its strong SOC and low nuclear spin.[10,11] Incorporating an atom with a higher atomic number like tin (Sn) into the crystal structure of Ge is expected to enhance the SOC further, therefore opening the research field toward Sn-based group-IV alloys. The incorporation of Sn also allows a large tunability of the electronic band structure from an indirect to a direct bandgap semiconductor, opening a new and attractive alternative to the current photonics,[12] electronics[13,14] and thermoelectrics fields.[15] The direct-bandgap also offers the ability to investigate spins of the high mobility Γ-electrons similar to III–V materials but with low nuclear spin of group-IV materials. The effective mass of the carriers in GeSn alloys also decreases with increasing Sn content, allowing for larger quantum dot sizes for spin-qubits and therefore, easier fabrication processes. Hence, the positive properties of both holes and electrons in GeSn make the alloy system worth investigating for spintronics.

Some recent works on phase-coherent transport,[16] coherent-spin dynamics,[17,18] angular negative magneto-resistance,[19] and 2-D hole gas conduction[20] indicate the promising potential of GeSn alloys for spin-based applications. In addition, theoretical findings suggest that GeSn is, for certain compositions, not only a Dirac-type semimetal but can also host signatures of Weyl nodes.[21–24] Here, the built-in chirality, in combination with

P. Kaul, O. Concepción, Q.-T. Zhao, D. Grützmacher, D. Buca
Peter Grünberg Institute – 9 (PGI-9)
Forschungzentrum Jülich
52428 Jülich, Germany
E-mail: p.kaul@fz-juelich.de; d.m.buca@fz-juelich.de
D. H. Wielens, C. Li, A. Brinkman
MESA+ Institute for Nanotechnology
University of Twente
Enschede 7522 NB, The Netherlands
P. Zellekens[+], K. Ishibashi
RIKEN Center for Emergent Matter Science
2-1, Hirosawa, Wako, Saitama 351-0198, Japan
P. Zellekens[+]
NTT Basic Research Laboratories
NTT Corporation
3-1 Morinosato-Wakamiya, Atsugi 243-0198, Japan

The ORCID identification number(s) for the author(s) of this article can be found under https://doi.org/10.1002/aelm.202400565

[+]Present address: School of Electronic and Electrical Engineering, University of Leeds, Leeds LS2 9JT, UK

© 2024 The Author(s). Advanced Electronic Materials published by Wiley-VCH GmbH. This is an open access article under the terms of the Creative Commons Attribution License, which permits use, distribution and reproduction in any medium, provided the original work is properly cited.

DOI: 10.1002/aelm.202400565

2199160x, 2025, 2, Downloaded from https://advanced.onlinelibrary.wiley.com/doi/10.1002/aelm.202400565 by Forschungszentrum Jülich GmbH Research Center, Wiley Online Library on [21/02/2025]. See the Terms and Conditions (https://onlinelibrary.wiley.com/terms-and-conditions) on Wiley Online Library for rules of use; OA articles are governed by the applicable Creative Commons License

superconducting contacts, has been proposed as a possible route toward topologically protected states for fault-tolerant quantum computation.[25–28] Despite the positive results, most of the literature still focuses on low Sn concentrations (<8 at.%) due to the challenges involved in the epitaxy of large Sn-content alloys.[29] However, recent advances in group-IV epitaxy allow the growth of high-crystal quality GeSn layers with Sn concentrations up to 17 at.%.[30–32]

Magneto-transport measurements at low temperatures point to the spintronics potential of direct-bandgap Sn-rich GeSn alloys and, to the best knowledge of the authors, have not been performed yet. At low temperatures, the transport regime in a semiconductor can change from classical diffusion to quantum diffusion, leading to quantum interference effects such as weak (anti-)localization (WL and WAL, respectively).[33] These effects manifest as sharp kinks in the resistance near zero magnetic field due to constructive (WL) and destructive (WAL) interference along closed scattering loops and allow the experimental extraction of the phase-coherence length L_Φ, which is a fundamental parameter of mesoscopic systems and therefore of high relevance for future spintronics and quantum devices. Furthermore, the Hall resistance behavior enables the extraction of carrier mobility to verify the theoretical prediction of mobility enhancement with Sn incorporation as a consequence of decreasing effective mass.[13]

Low-temperature magneto-transport measurements in epitaxial n-type (phosphorous) doped GeSn layers with Sn concentrations up to 14 at.% are presented in this work. WL effects are observed and, by using the Hikami-Larkin-Nagaoka (HLN) model, phase coherence lengths of the order of hundred nanometers were extracted, similar to heavily doped Si. For the highest Sn content layers, Shubnikov de Haas (SdH) oscillations have been observed and subsequently used to extract the effective Γ-electron mass. Moreover, a clear trend of mobility enhancement is observed for increasing Sn incorporation, showing the advantages of these materials for nano-electronic devices. The results provide clear proof of robust phase-coherent transport in direct-bandgap Sn-rich GeSn alloys and thus make it a promising building block for spintronics applications and superconducting devices.

2. Epitaxial Growth and Device Fabrication

The goal is to epitaxially grow GeSn alloys with a doping level that offers an electron population in the Γ-valley, i.e., at the center of the Brillouin-Zone, and thus enable the investigation of their properties. Epitaxially, this can be achieved by *in-situ* n-type doping of the GeSn thin film. The strategy followed in this work is the growth of a thick partial strain-relaxation GeSn buffer, followed by the deposition of the n-type phosphorus-doped GeSn (GeSn:P) layer of interest.

The investigated samples are grown on 200 mm Si (100) wafers using an industrial reduced-pressure chemical vapor deposition (RP-CVD) reactor. Prior to the thick GeSn buffer layer growth, 500 nm of Ge is deposited to compensate for the large lattice mismatch relative to the Si substrate underneath. Ge_2H_6 and $SnCl_4$ are used as Ge and Sn precursors, respectively, and the Sn concentration is tuned by varying the temperature and the gas flow rate at a constant reactor pressure. Details related to the growth can be found elsewhere.[29,30] On top of the GeSn buffer layer, a 50 nm highly-relaxed n-type doped GeSn:P layer is epitaxially grown using the same process temperature and PH_3 as an additional gas precursor. A physical description of the grown layers discussed here is given in **Table 1**.

The alloys' stoichiometry, thickness, and crystal quality were obtained by Rutherford backscattering spectrometry (RBS) in random and channeling configurations (see Figure S1a of the Supporting Information (SI) file). The lattice strain in the layers was extracted from X-ray diffraction (XRD) spectra around the (004) symmetric reflection in $\omega/2\theta$ geometry and completed by asymmetric (224) reciprocal space maps (RSM) (**Figure 1a,b**). The GeSn peak shifts to lower 2θ angles through the substitutional incorporation of Sn atoms into the Ge lattice, resulting in larger lattice parameters. The presence of two peaks is typical for thick GeSn layers, where above the critical thickness for relaxation, the Sn content incorporation increases.[29] The RSM of the 12 at.% Sn sample (Figure 1b) shows a high lattice strain relaxation with the GeSn peak close to the cubic line. The strain relaxation of the epitaxial built-up biaxial compressive strain and the Sn composition define the conduction band alignment in the GeSn alloys and consequently the indirect or direct nature of the bandgap.[34] A high crystalline quality of the samples is obtained and is highlighted here for the 12 at.% Sn sample by high-resolution transmission electron micrograph (HR-TEM) image (background of Figure 1b) taken in the middle of the $Ge_{0.88}Sn_{0.12}$ layer.

The electrically active P concentration measured by electrochemical capacitance-voltage (ECV) profiling is plotted in Figure 1c. The phosphorous concentrations in the top GeSn:P layers are in the 10^{19} at. cm^{-3} range (full symbols), while the as-grown GeSn buffers show a p-type behavior equivalent to a doping concentration of 10^{17}–10^{18} at. cm^{-3} (empty symbols). This p-type doping is characterized in the next section (also see Supporting Information) and is caused by the misfit dislocations at the GeSn/Ge interface and by the presence of point defects (typically vacancies) created during the epitaxial growth which are needed to mediate the incorporation of the larger Sn atoms volume in the Ge lattice.

The electronic band structure around the Γ-point, including the effects of strain, was calculated using the 8-band k·p method and this was used to find the electron effective mass.[35] The k.p parameters for the alloy are calculated using the interpolation expressions given in reference.[36] For other parameters – deformation potentials and band gaps (including those for the L-valley), the elemental data is collected in Table I of reference[37] and the alloy interpolation expressions are given there as well. The electron distribution over Γ- and L- valleys was calculated using the anisotropic/nonparabolic k·p dispersion around the Γ-point and effective mass approximation for the L-valley. The Γ- and L-valley energies versus the Sn content and the lattice strain are presented in Figure 1d. The top valence band was taken as zero energy. The intersection of the Γ- and L-valley energy planes represents the (Sn, at.%; ϵ, strain) condition at the indirect to direct bandgap transition. The energy difference between the Γ- and L- valleys energies, called "directness," determines the number of electrons residing in the two valleys.

At 5K and low electron density, all electrons are populating the lowest energy valley, which is the L-valley for indirect bandgap GeSn alloys and Γ-valley for the direct bandgap case (Figure 1e). For elevated doping levels, the electrons will be distributed between the two valleys according to their energy position and the

 © 2024 The Author(s). Advanced Electronic Materials published by Wiley-VCH GmbH

Table 1. Overview of the GeSn:P/GeSn/Si layers under investigation: Sn concentration and thickness measured by RBS; strain values estimated by XRD-RSM, and carrier concentration (n) obtained by ECV.

Sn content [at.%]	GeSn buffer		Top GeSn:P		Lattice strain (%)
	thickness [nm]	p [x10^{17} cm^{-3}]	thickness [nm]	n [x10^{19} cm^{-3}]	
7	280	3	46	5	−0.26
8.5	294	6	56	4	−0.26
10	329	9	50	10	−0.3
12	279	22	40	3.5	−0.44
14	364	11	56	3	−0.55

corresponding density of states (DOS). As shown in Figure 1e, even if the GeSn layer has a direct bandgap, the proximity of the L-valley and its much larger DOS will lead to a low electron concentration in the Γ-valley. However, it is still possible to detect signals of their smaller mass and high mobility, e.g. by means of the SdH effect and analyzing the oscillations on top of the classical L-electrons background, as will be discussed below. In addition, the presence of the biaxial strain deforms the shape of the constant energy surface, leading to in-plane (y,x) and out-of-plane (z) mass anisotropy. The large doping levels shift the electrons Fermi level up in the Γ-valley and the band non-parabolicity leads to larger effective masses than are typically calculated theoretically for the bottom of the Γ-valley (k = 0).

3. Results and Discussion

Hall-bar geometry devices are fabricated using standard Si cleanroom process technology. A top-view scanning electron microscope image (SEM) is shown in Figure 1f and a detailed description of the fabrication process is available in Figure S2 (Supporting Information). Magneto-transport measurements are performed in the presence of a perpendicular magnetic field up to 9 T in the temperature range between 100 mK and 300 K. An excitation current is applied along the device and the longitudinal and transversal measured voltages (V_{xx} and V_{xy}) are used to calculate the longitudinal (R_{xx}) and Hall (R_{xy}) resistances, respectively.

For the sake of conformity and comparison, we have also studied a GeSn layer without a top n-type doped layer. The magnetoresistance ($MR = (\frac{R_{xx}(B) - R_{xx}(0)}{R_{xx}(0)}) \times 100\%$) and Hall resistance at 2 K of the as-grown $Ge_{0.86}Sn_{0.14}$ sample is presented in Figure 1f. The WAL effect, represented by a dip in the MR around zero magnetic fields, is observed for the as-grown sample, consistent with previous literature data for p-type Ge and GeSn layers.[16,38] The Hall resistance shows a positive slope, confirming that the conductivity is provided by holes, and its nonlinearity with the magnetic field alludes to the presence of light-hole and heavy-hole bands in GeSn.[13] The complete temperature dependence along with the R_{xx} plots are provided in Figure S1b,d (Supporting Information). The resistance at 2 K is ≈12 kΩ and the low p-type carrier concentration of 3×10^{17} at. cm^{-3} (Figure S1e, Supporting Information) is expected to form a p-n junction with the doped n-GeSn layer, resulting in reduced parallel conduction in the GeSn:P/GeSn structures. Hence, in the measurements below, only the GeSn:P layers are considered due to being the primary conduction channel. However, for a complete analysis, the role of the GeSn buffer must also be considered which is outside the capabilities of this work.

3.1. Doped n-GeSn Samples

Magneto-transport measurements for the GeSn:P layers are presented in **Figure 2**. The WL effect, indicating diffusive phase-coherent transport, is present for all Sn concentrations (Figure 2a; Figure S3a,b, Supporting Information), while the Hall resistance slope is negative, confirming electron conduction in the n-GeSn layers (Figure 2c). The MR value increases with the Sn incorporation, indicating electron mobility enhancement as $MR \propto (\mu B)^2$.[39] The 12–14 at.% Sn samples show non-linearity in Hall resistance under high magnetic fields indicating dual electron transport channels, namely contributions from the L- and Γ-valley electrons. However, for comparison with the literature, a single-channel transport approximation is used to estimate average mobility. The averaged electron mobility from MR and R_{xy} data increases consistently with Sn concentration from 200 to 700 cm^2 V^{-1} s^{-1} (see Figure S3f, Supporting Information). Benchmarking over literature values of 105, 300, and 100 cm^2 V^{-1} s^{-1} for electron mobilities at doping concentrations in the range of 10^{19} cm^{-3} in n-Si,[40] n-Ge,[38] and n-GeSn (8 at.% Sn)[16] respectively, the values extracted here are much higher and in agreement with the theoretical prediction of mobility enhancement with Sn incorporation.[13] The dual-channel model for accurate analysis will be used in the next section.

The WL effect vanishes above 25 K and a conventional parabolic positive MR (R_{xx} in Figure S3e, Supporting Information) is observed as the transport regime changes from quantum-diffusive to classical diffusive (Figure 2b). Above the same temperature, the Hall resistance oscillations present at high magnetic fields also disappear (Figure 2d), which is attributed to the reduction of Γ-electron over L- electron population caused by increased inelastic intra-band valley scattering due to the low energy separation (Figure 1d) and also thermal broadening causing loss of quantization to observe such oscillations.

For applications based on quantum-mechanical spin effects, phase-coherent transport is an essential requirement demanding large phase-coherence lengths (L_Φ). This parameter is extracted using the reduced HLN formalism, by fitting the WL contribution to the magneto-conductance.[41] The Sn-dependent phase-coherence lengths for three different temperatures are plotted in

© 2024 The Author(s). Advanced Electronic Materials published by Wiley-VCH GmbH

2199160x, 2025, 2, Downloaded from https://advanced.onlinelibrary.wiley.com/doi/10.1002/aelm.202400565 by Forschungszentrum Jülich GmbH Research Center, Wiley Online Library on [21/02/2025]. See the Terms and Conditions (https://onlinelibrary.wiley.com/terms-and-conditions) on Wiley Online Library for rules of use; OA articles are governed by the applicable Creative Commons License

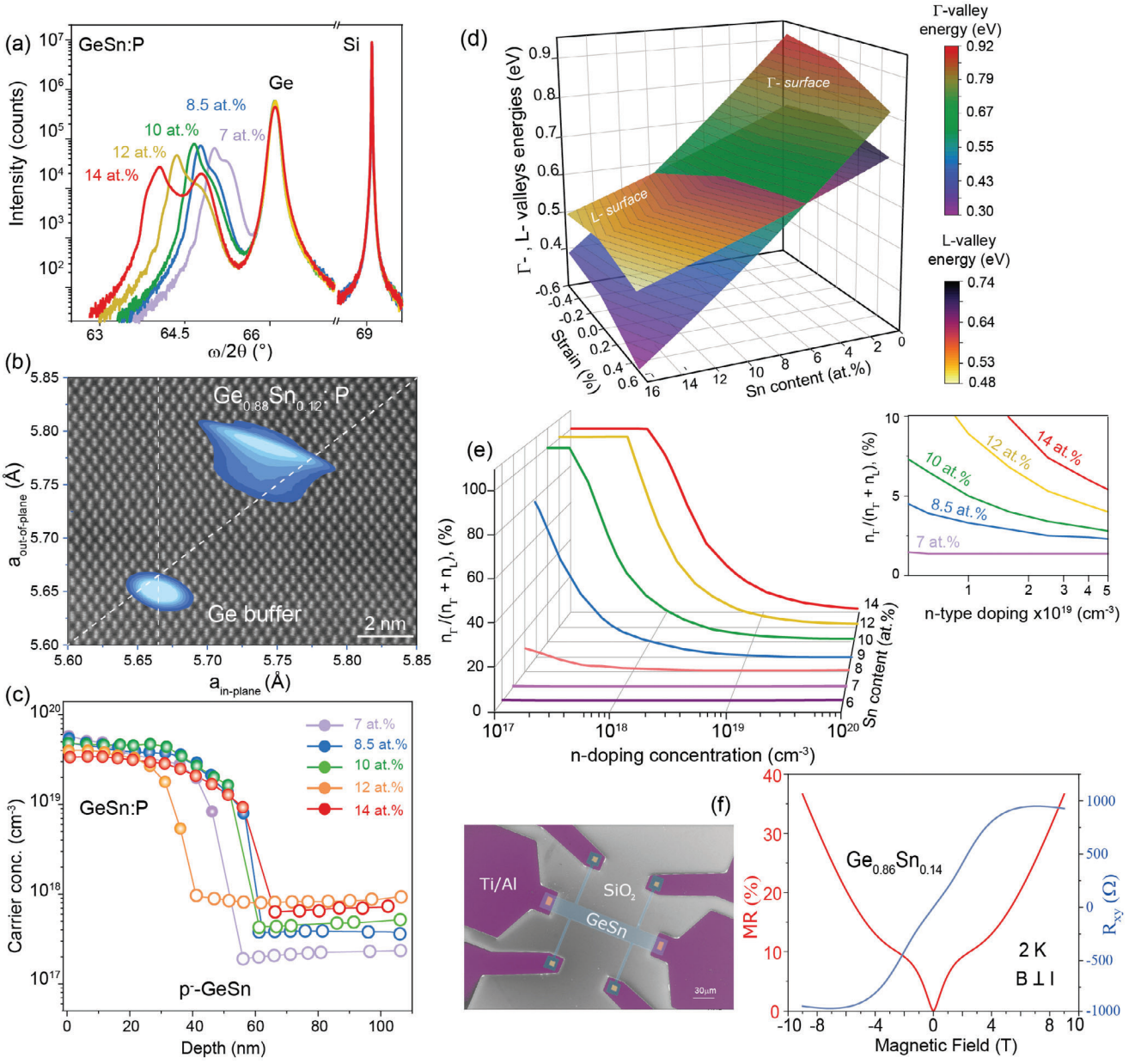

Figure 1. Material characterization a) Symmetric (004) XRD ω-2θ spectra of different Sn content GeSn:P structures. b) Asymmetric (224) RSM overlapped with a HR-TEM micrograph of the $Ge_{0.88}Sn_{0.12}$ layer. The vertical and diagonal dotted lines indicate the pseudomorphic to the Ge lattice and cubic crystal lines, respectively. c) Carrier concentration depth profiles of the GeSn:P/GeSn structures. d) Calculated Γ- and L-valley energies at 5K as a function of Sn concentration and lattice strain. The intersection line shows the conditions where the GeSn layers change from indirect to direct bandgap semiconductor. e) Doping dependent electron population of Γ-valley for cubic GeSn layers with different Sn content. f) Top-view SEM image of the Hall bar device and the measured MR (red) and Hall resistance (blue) at 2 K as a function of the applied magnetic field for undoped $Ge_{0.86}$ $Sn_{0.14}$ sample.

Figure 2e where coherence length as large as 150 nm is extracted at 2 K and decreases in value with increasing temperature due to the enhancement of the inelastic scattering. However, even at 15 K, it is larger than the layer thickness, a condition for the use of the 2D HLN theory. The measured L_Φ values are larger than the literature-reported values of 120 nm for GeSn (8 at.% Sn) and show no decreasing trend with Sn incorporation.[16] Measurements performed in a dilution refrigerator in the mK temperature regime lead to an increase of the phase-coherence length up to 400 nm as shown in Figure 2f for the 12 at.% Sn sample. Such L_Φ is comparable to the one obtained in standard materials used nowadays in spintronics, such as heavily doped Si, Ge, and GaAs at similar temperatures.[42,43] These results show the feasibility of exploiting advantages such as high SOC, and lower effective mass by incorporating Sn in Ge without loss in phase-coherence and form the first steps toward spin-active devices and applications in topological quantum computation based on Sn-rich group-IV materials.

© 2024 The Author(s). Advanced Electronic Materials published by Wiley-VCH GmbH

2199160x, 2025, 2, Downloaded from https://advanced.onlinelibrary.wiley.com/doi/10.1002/aelm.202400565 by Forschungszentrum Jülich GmbH Research Center, Wiley Online Library on [21/02/2025]. See the Terms and Conditions (https://onlinelibrary.wiley.com/terms-and-conditions) on Wiley Online Library for rules of use; OA articles are governed by the applicable Creative Commons License

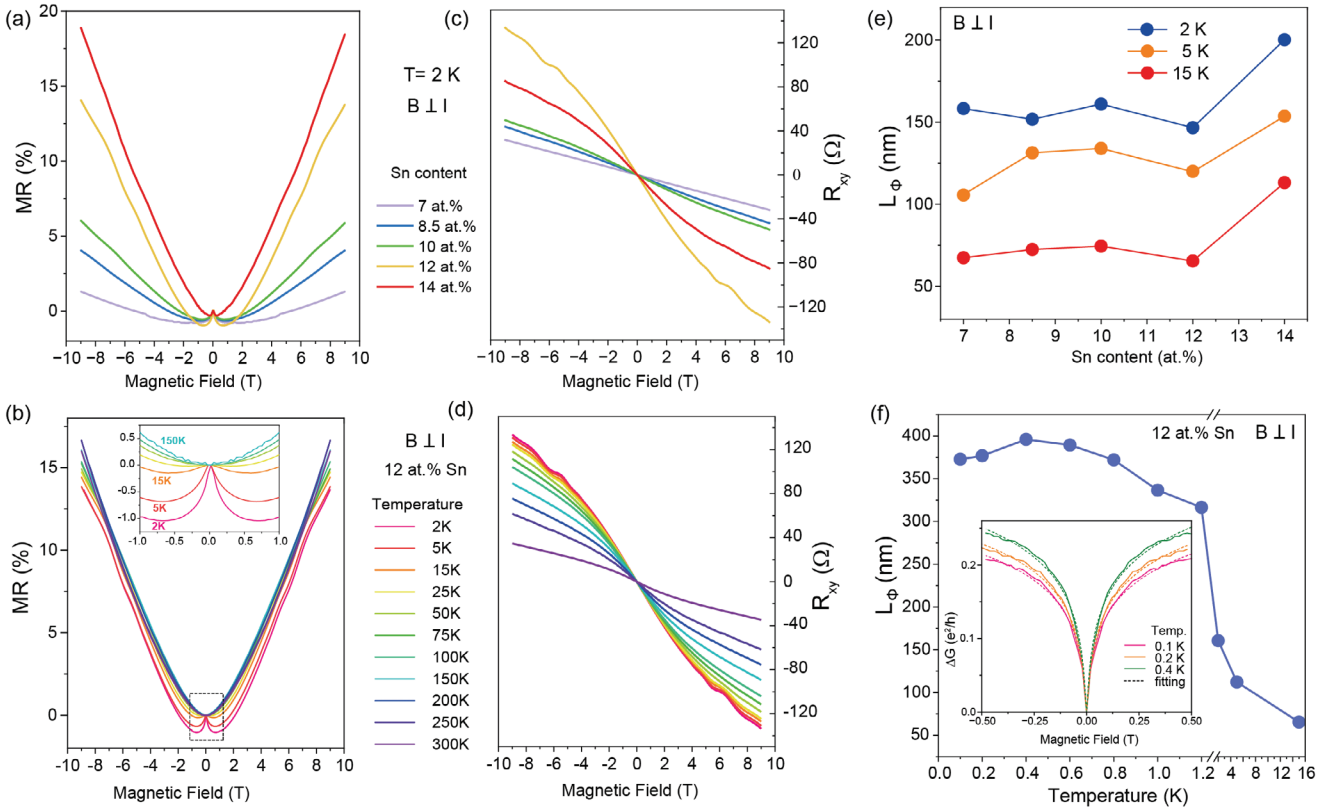

Figure 2. Phase coherence measurements. a) MR and c) Hall resistance as a function of the applied magnetic field at 2K for the GeSn:P samples with different Sn contents. Temperature dependence of the b) MR and d) R_{xy} for the $Ge_{0.88}Sn_{0.12}$ sample. Phase coherence lengths extracted from the WL fitting using the reduced HLN model e) as a function of Sn concentration and f) as a function of temperature for the $Ge_{0.88}Sn_{0.12}$ sample (HLN fitting in the inset).

3.2. Effective Mass of Electrons in GeSn Alloys

Shubnikov-de Haas (SdH) oscillations offer additional information regarding material properties such as the effective mass of electrons, their mobility, and concentration. The oscillations, attributed to the low mass high mobility Γ-valley electrons, are isolated from the strong classical background using over-smoothing of the data to approximate the classical background, similar to the approach used by Li et al.[44] (details in Supporting Information). The extracted dR_{xx} signal at different temperatures shows a clear periodic modulation of the resistance in dependence on the inverse of the magnetic field $1/B$. This is presented in **Figure** 3a,b for the samples with high Sn content. The frequency extracted from the oscillations is found to be 19.4 and 13.4 T for the 12 and 14 at.% Sn alloys, respectively. Using this frequency ($f_{1/B}$), the 3-D carrier concentration is estimated to be in the range of 6–9 × 10^{16} at. cm^{-3} for the samples with the following equation:

$$n_{2D} = \frac{f_{1/B} e}{h} \quad n_{3D} = \frac{n_{2D}}{t} \tag{1}$$

where, n_{2D} is the 2-D carrier concentration, e the electron charge, h the Planck's constant, and t the layer thickness which in this case is 50 nm. The low carrier concentration compared to the total doping level is explained by the low population of Γ-valley electrons over the L-valley as shown in Figure 1e.

The temperature dependence of SdH oscillations allows the extraction of the effective mass of Γ-electrons using the Dingle equation,[44] which can subsequently be fitted using the following expression:[45]

$$\ln\left(\frac{dR_{xx}}{T}\right) = C - \left[\sinh\left(\frac{2\pi^2 k_B T m_{eff}}{e\hbar B}\right)\right] \tag{2}$$

where C is a fitting parameter, k_B is the Boltzmann constant, m_{eff} the carrier effective mass, and $\hbar$ the reduced Planck's constant. The fits correspond to the different peaks of the samples with 12 at.% and 14 at.% Sn are shown in Figure 3c,d. The extracted averaged effective masses are 0.055 m_0 and 0.034 m_0 for 12 and 14 at.% Sn samples, respectively. Both values are smaller than the calculated value of 0.079 m_0 for L-electrons in GeSn, showing that the Γ-electrons are responsible for the presence of the SdH oscillations. This is further supported by the measurements on indirect bandgap GeSn alloys, e.g. the sample with 7 at.% Sn, showing no SdH oscillations in R_{xx} and R_{xy} resistances down to 100 mK and single electron conduction channel based on L-electrons (Figure S4f, Supporting Information).

From the theoretical calculations, the Fermi surface for GeSn:P at low temperatures is found to be spherical and located at the center of the Brillouin zone, which results in an isotropic behavior with m_{eff} = 0.033 m_0. For strained layers, the Fermi sur-

© 2024 The Author(s). Advanced Electronic Materials published by Wiley-VCH GmbH

2199160x, 2025, 2, Downloaded from https://advanced.onlinelibrary.wiley.com/doi/10.1002/aelm.202400565 by Forschungszentrum Jülich GmbH Research Center, Wiley Online Library on [21/02/2025]. See the Terms and Conditions (https://onlinelibrary.wiley.com/terms-and-conditions) on Wiley Online Library for rules of use; OA articles are governed by the applicable Creative Commons License

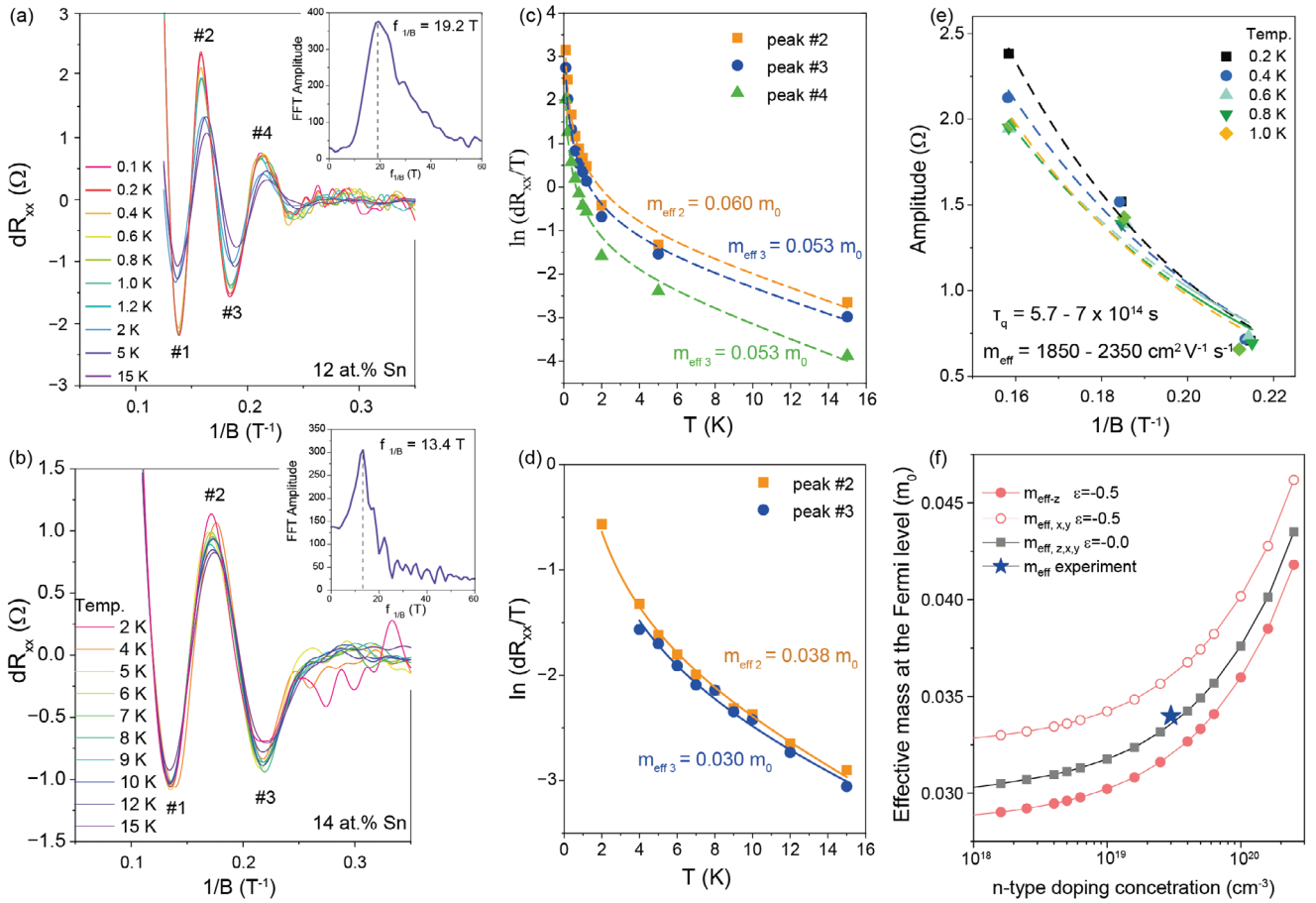

Figure 3. SdH oscillations in n-type GeSn. Isolated Shubnikov-de Haas oscillations from the longitudinal resistance curves plotted as a function of *1/B* for the a) 12 at.% and b) 14 at.% Sn samples, respectively. Extracted frequency of the oscillations using FFT is shown in the insets. c,d) Effective mass fitting from the Dingle equation and temperature dependence of oscillation peaks of a,b). Mass values are in free electron mass units (m_0). e) Quantum scattering time fitting using the field-dependent decay of oscillation amplitudes at different temperatures. f) Calculated effective mass at the Fermi level as a function of the n-type doping concentration.

face is deformed, which leads to an anisotropy between in-plane and out-of-plane orientation. For n-type doped layers, the effective mass is calculated at E_F (T = 0K) (which we assume to be a reasonable approximation for temperature ranges T < 5K) and by taking into account the band non-parabolicity. The Γ-electrons effective mass of 0.034 m_0 for the $Ge_{0.86}Sn_{0.14}$ sample under the biaxial compressive strain of −0.5% and phosphorus doping level of 3×10^{19} at. cm^{-3}, is ≈15% larger than the lowest calculated out-of-plane effective mass (*z*-direction) $m_{eff}^{z} = 0.032\ m_0$, but below the in-plane effective mass (x,y directions) $m_{eff}^{x,y} = 0.036\ m_0$ (see Figure 3f). However, surprisingly the effective mass of the 12 at.% Sn sample, which shows multiple and clear oscillations, is ≈48% larger than the theoretical value, a discrepancy that is not easy to explain by material parameters or potential simulation-model inaccuracies. Despite the discrepancy, all of the different samples measured report masses that are much smaller than the L-electron effective mass (Figure S5e, Supporting Information).

The presence of four peaks for the 12 at.% Sn sample in Figure 3a, enables the extraction of the quantum scattering time (τ_q) using the exponential part ($e^{-\frac{\pi m_{eff}}{e\tau_q B}}$) of the Dingle equation, resulting in a value of $\tau_q = 5 \times 10^{-14}$ s at 0.2 K and 7×10^{-14} s at 0.6 K (Figure 3e) that leads to the calculation of the Γ-electrons mobility 1850 $cm^2\ V^{-1}\ s^{-1}$ at 0.2K and 2350 $cm^2\ V^{-1}\ s^{-1}$ at 0.6 K. Using the carrier concentration and mobility extracted previously from the SdH analysis, the L-contribution can be estimated using a dual-channel model fitting of R_{xy}.[46] The L-electron concentration of $\approx 1 \times 10^{19}$ at. cm^3 and Hall mobility value of 200 $cm^2\ V^{-1}\ s^{-1}$ are obtained, close to the previously measured mobility of the 7 at.% Sn sample. Hence, the mobility measured by the single channel model is an averaged value of the 2000 and 200 $cm^2\ V^{-1}\ s^{-1}$ mobility of Γ- and L- electrons, respectively. The measurements presented above have been performed and reproduced in all 3 laboratories involved in this work using different measurement setups (Figure S5c,d, Supporting Information).

While the onset of the Γ-valley electron population with increasing Sn incorporation is clearly shown, as well as their low effective masses, future efforts are required to extend the analysis of Γ-valley electrons. Low n-doped carrier concentration and large directness that allows only Γ-valley occupation is preferred. The low carrier density will also increase the mobility and allow for significant gate control to manipulate the spin. To study the

© 2024 The Author(s). Advanced Electronic Materials published by Wiley-VCH GmbH

2199160x, 2025, 2, Downloaded from https://advanced.onlinelibrary.wiley.com/doi/10.1002/aelm.202400565 by Forschungszentrum Jülich GmbH Research Center, Wiley Online Library on [21/02/2025]. See the Terms and Conditions (https://onlinelibrary.wiley.com/terms-and-conditions) on Wiley Online Library for rules of use; OA articles are governed by the applicable Creative Commons License

spin-orbit related phenomena, e.g., WAL, and get a better understanding of the phase coherence and spin-orbit scattering length, similar experiments must be performed in p-type GeSn alloys. Future studies on Sn-based heterostructures with stronger confinement and better spatial localization of the transport channel must be conducted to achieve 2D conduction for holes and electrons. The 2-D conduction is a crucial requirement for the investigation of future spin-qubit or hybrid qubit devices in order to reveal the alloy system's true potential for quantum computing.

4. Conclusion

Epitaxial n-type high Sn content GeSn alloys have been investigated using magneto-transport measurements. The observation and analysis of weak (anti-) localization can be associated with robust phase-coherent transport with long coherence lengths of ≈400 nm at 100 mK. In addition, for high Sn concentrations, Shubnikov-de Haas oscillations were measured, showing signatures of a superposition of two distinct transport channels. The latter is interpreted as a decoupling of the Γ-valley and L-valley electrons, robustly proving the Γ-valley conduction in group-IV materials with the 14 at.% Sn content sample showing an effective mass of 0.034 m_0 and a mobility of 2000 $cm^2\ V^{-1}\ s^{-1}$. The large phase-coherence length, low effective mass, and high mobility prove theoretical predictions and indicate the potential usefulness of GeSn for nanoelectronics and spintronics. The framework presented in this work is the first step toward investigating direct-bandgap GeSn alloys and sets forward future experimentation to be performed in order to achieve a comprehensive understanding of their potential in novel spin-based and quantum computing applications.

5. Experimental Section

Equations used for parameter extraction (full explanation in Supporting Information).

HLN for L_Φ:

$$\Delta G = \frac{e^2}{2\pi^2\hbar}\left[\psi\left(\frac{1}{2}+\frac{\hbar}{4eBL_\Phi^2}\right)-\ln\left(\frac{\hbar}{4eBL_\Phi^2}\right)\right] \tag{3}$$

Single channel Hall mobility:

$$\sigma = \frac{L}{R_{xx}\,(B=0)\,Wt} \quad n = \left(\frac{R_{xy}}{B}\right)^{-1}\frac{1}{te} \quad \mu = \frac{\sigma}{ne} \tag{4}$$

Dingle Equation:

$$dR_{xx/xy} = A\,\frac{\frac{2\pi^2 k_B T m_{\text{eff}}}{e\hbar B}}{\sinh\left(\frac{2\pi^2 k_B T m_{\text{eff}}}{e\hbar B}\right)}\exp\left(-\frac{\pi B m_{\text{eff}}}{e\tau_q}\right) \tag{5}$$

Dual channel Hall resistance:

$$R_{xy} = \frac{1}{e}\,\frac{(p_1{\mu_1}^2+p_2{\mu_2}^2)+{\mu_1}^2{\mu_2}^2\,(p_1+p_2)\,B^2}{\left(|p_1|\,\mu_1+|p_2|\,\mu_2\right)^2+{\mu_1}^2{\mu_2}^2(p_1+p_2)^2B^2}B \tag{6}$$

Supporting Information

Supporting Information is available from the Wiley Online Library or from the author.

Acknowledgements

The authors would like to express gratitude toward Dr. Shibabrata Nandi and Berthold Schmitz of PGI-4/JCNS-2 in Forschungzentrum Jülich for their assistance in low-temperature magneto-transport measurements. The authors acknowledge financial support from the European Commission for the LASTSTEP Project under grant agreement 101070208 and from the Japan Science and Technology Agency (JST) as part of Adopting Sustainable Partnerships for Innovative Research Ecosystem (ASPIRE), Grant Number JPMJAP2338.

Conflict of Interest

The authors declare no conflict of interest.

Data Availability Statement

The data that support the findings of this study are available from the corresponding author upon reasonable request.

Keywords

GeSn alloys, group IV semiconductors, magneto-transport, spintronics, topological

Received: July 19, 2024
Revised: September 25, 2024
Published online: November 1, 2024

[1] D. Loss, D. P. DiVincenzo, *Phys. Rev. A (Coll Park)* **1998**, *57*, 120.
[2] G. Burkard, T. D. Ladd, J. M. Nichol, A. Pan, J. R. Petta, *Rev. Mod. Phys.* **2021**, *95*, 025003.
[3] Y. Fang, P. Philippopoulos, D. Culcer, W. A. Coish, S. Chesi, *Mater. Quantum Technol.* **2023**, *3*, 012003.
[4] J. Shalf, *Philos. Transact. Royal Soc. A* **2020**, *378*, 20190061.
[5] H. Bluhm, S. Foletti, I. Neder, M. Rudner, D. Mahalu, V. Umansky, A. Yacoby, *Nat. Phys.* **2010**, *7*, 109.
[6] A. M. Tyryshkin, S. Tojo, J. J. L. Morton, H. Riemann, N. V. Abrosimov, P. Becker, H. J. Pohl, T. Schenkel, M. L. W. Thewalt, K. M. Itoh, S. A. Lyon, *Nat. Mater.* **2011**, *11*, 143.
[7] J. Yoneda, K. Takeda, T. Otsuka, T. Nakajima, M. R. Delbecq, G. Allison, T. Honda, T. Kodera, S. Oda, Y. Hoshi, N. Usami, K. M. Itoh, S. Tarucha, *Nat. Nanotechnol.* **2017**, *13*, 102.
[8] R. Jansen, *Nat. Mater.* **2012**, *11*, 400.
[9] M. Pioro-Ladrière, T. Obata, Y. Tokura, Y. S. Shin, T. Kubo, K. Yoshida, T. Taniyama, S. Tarucha, *Nat. Phys.* **2008**, *4*, 776.
[10] G. Scappucci, C. Kloeffel, F. A. Zwanenburg, D. Loss, M. Myronov, J. J. Zhang, S. De Franceschi, G. Katsaros, M. Veldhorst, *Nat. Rev. Mater.* **2020**, *6*, 926.
[11] H. Watzinger, J. Kukučka, L. Vukušić, F. Gao, T. Wang, F. Schäffler, J. J. Zhang, G. Katsaros, *Nat. Commun.* **2018**, *9*, 3902.
[12] S. Wirths, R. Geiger, N. von den Driesch, G. Mussler, T. Stoica, S. Mantl, Z. Ikonic, M. Luysberg, S. Chiussi, J. M. Hartmann, H. Sigg, J. Faist, D. Buca, D. Grützmacher, *Nature Photonics* **2015**, *9*, 88.

© 2024 The Author(s). Advanced Electronic Materials published by Wiley-VCH GmbH

2199160x, 2025, 2, Downloaded from https://advanced.onlinelibrary.wiley.com/doi/10.1002/aelm.202400565 by Forschungszentrum Jülich GmbH Research Center, Wiley Online Library on [21/02/2025]. See the Terms and Conditions (https://onlinelibrary.wiley.com/terms-and-conditions) on Wiley Online Library for rules of use; OA articles are governed by the applicable Creative Commons License

[13] C. Schulte-Braucks, RWTH Aachen University, **2017**.
[14] Y. Junk, O. Concepción, M. Frauenrath, J. Sun, J. H. Bae, F. Bärwolf, A. Mai, J. Hartmann, D. Grützmacher, D. Buca, Q. Zhao, *Adv. Electr. Mater. Portico*. **2010**, https://doi.org/10.1002/aelm.202400561.
[15] O. Concepción, J. Tiscareño-Ramírez, A. A. Chimienti, T. Classen, A. A. Corley-Wiciak, A. Tomadin, D. Spirito, D. Pisignano, P. Graziosi, Z. Ikonic, Q. T. Zhao, D. Grützmacher, G. Capellini, S. Roddaro, M. Virgilio, D. Buca, *ACS App. Energy Mater.* **2024**, *7*, 4394.
[16] D. Weißhaupt, H. S. Funk, M. Kern, M. M. Dettling, D. Schwarz, M. Oehme, C. Sürgers, J. Van Slageren, I. A. Fischer, J. Schulze, *J. Phys.: Condens. Matter* **2020**, *33*, 085703.
[17] S. De Cesari, A. Balocchi, E. Vitiello, P. Jahandar, E. Grilli, T. Amand, X. Marie, M. Myronov, F. Pezzoli, *Phys. Rev. B* **2019**, *99*, 035202.
[18] A. Marchionni, C. Zucchetti, F. Ciccacci, M. Finazzi, H. S. Funk, D. Schwarz, M. Oehme, J. Schulze, F. Bottegoni, *Appl. Phys. Lett.* **2021**, *118*, 212402.
[19] K. Shu, N. Wang, N. Huo, F. Wan, J. Li, C. Xue, *ACS Appl. Mater. Interfaces* **2021**, *13*, 29960.
[20] C.-T. Tai, P.-Y. Chiu, C.-Y. Liu, H.-S. Kao, C. T. Harris, T.-M. Lu, C.-T. Hsieh, S.-W. Chang, J.-Y. Li, C.-T. Tai, P.-Y. Chiu, C.-Y. Liu, H.-S. Kao, J.-Y. Li, C. T. Harris, T.-M. Lu, C.-T. Hsieh, S.-W. Chang, *Adv. Mater.* **2021**, *33*, 2007862.
[21] B. Q. Lv, N. Xu, H. M. Weng, J. Z. Ma, P. Richard, X. C. Huang, L. X. Zhao, G. F. Chen, C. E. Matt, F. Bisti, V. N. Strocov, J. Mesot, Z. Fang, X. Dai, T. Qian, M. Shi, H. Ding, *Nat. Phys.* **2015**, *11*, 724.
[22] S. Y. Xu, I. Belopolski, D. S. Sanchez, C. Zhang, G. Chang, C. Guo, G. Bian, Z. Yuan, H. Lu, T. R. Chang, P. P. Shibayev, M. L. Prokopovych, N. Alidoust, H. Zheng, C. C. Lee, S. M. Huang, R. Sankar, F. Chou, C. H. Hsu, H. T. Jeng, A. Bansil, T. Neupert, V. N. Strocov, H. Lin, S. Jia, M. Z. Hasan, *Sci. Adv.* **2015**, *1*, 1501092.
[23] X. Kong, L. Li, F. M. Peeters, *Appl. Phys. Lett.* **2018**, *112*, 251601.
[24] W. Cao, P. Tang, S. C. Zhang, W. Duan, A. Rubio, *Phys. Rev. B* **2016**, *93*, 241117.
[25] Z. S. Gao, X.-J. Gao, W.-Y. He, X. Y. Xu, T. K. Ng, K. T. Law, *Quant. Front.* **2022**, *1*, 3.
[26] M. Sato, S. Fujimoto, *J. Phys. Soc. Jpn.* **2016**, *85*, 072001.
[27] M. Z. Hasan, G. Chang, I. Belopolski, G. Bian, S. Y. Xu, J. X. Yin, *Nat. Rev. Mater.* **2021**, *6*, 784.
[28] S. Wang, B. C. Lin, A. Q. Wang, D. P. Yu, Z. M. Liao, *Adv Phys X* **2017**, *2*, 518.
[29] N. von den Driesch, RWTH Aachen University, **2018**.
[30] O. Concepción, N. B. Søgaard, J. H. Bae, Y. Yamamoto, A. T. Tiedemann, Z. Ikonic, G. Capellini, Q. T. Zhao, D. Grützmacher, D. Buca, *ACS Appl. Electron. Mater.* **2023**, *5*, 2268.
[31] M. R. M. Atalla, S. Assali, A. Attiaoui, C. Lemieux-Leduc, A. Kumar, S. Abdi, O. Moutanabbir, M. R. M. Atalla, S. Assali, A. Attiaoui, C. Lemieux-Leduc, A. Kumar, S. Abdi, O. Moutanabbir, *Adv. Funct. Mater.* **2021**, *31*, 2006329.
[32] J. Chrétien, Q. M. Thai, M. Frauenrath, L. Casiez, A. Chelnokov, V. Reboud, J. M. Hartmann, M. El Kurdi, N. Pauc, V. Calvo, *Appl. Phys. Lett.* **2022**, *120*, 51107.
[33] H.-Z. Lu, S.-Q. Shen, **2014**, *9167*, 263.
[34] S. Gupta, B. Magyari-Köpe, Y. Nishi, K. C. Saraswat, *J. Appl. Phys.* **2013**, *113*, 73707.
[35] T. B. Bahder, *Phys. Rev. B* **1990**, *41*, 11992.
[36] S. Q. Liu, S. T. Yen, *J. Appl. Phys.* **2019**, *125*, 245701.
[37] D. Rainko, Z. Ikonic, N. Vukmirović, D. Stange, N. von den Driesch, D. Grützmacher, D. Buca, *Sci. Rep.* **2018**, *8*, 15557.
[38] P. J. Newton, R. Mansell, S. N. Holmes, M. Myronov, C. H. W. Barnes, *Appl. Phys. Lett.* **2017**, *110*, 62101.
[39] V. A. Johnson, W. J. Whitesell, *Phys. Rev.* **1953**, *89*, 941.
[40] N. D. Arora, J. R. Hauser, D. J. Roulston, *IEEE Trans. Electron Devices* **1982**, *29*, 292.
[41] S. Hikami, A. I. Larkin, Y. Nagaoka, *Progr. Theoret. Phys.* **1980**, *63*, 707.
[42] S. Shamim, S. Mahapatra, G. Scappucci, W. M. Klesse, M. Y. Simmons, A. Ghosh, *Sci. Rep.* **2017**, *7*, 46670.
[43] J. Duan, C. Wang, L. Vines, L. Rebohle, M. Helm, Y. J. Zeng, S. Zhou, S. Prucnal, *New J. Phys.* **2021**, *23*, 083034.
[44] C. Li, J. C. de Boer, B. de Ronde, S. V. Ramankutty, E. van Heumen, Y. Huang, A. de Visser, A. A. Golubov, M. S. Golden, A. Brinkman, *Nat. Mater.* **2018**, *17*, 875.
[45] S. F. Feste, S. Mantl, *Physical Investigations of Novel Materials and Structures for Nano-MOSFETs*, Publikationsserver der RWTH Aachen University, Aachen **2009**.
[46] J. S. Kim, S. S. A. Seo, M. F. Chisholm, R. K. Kremer, H. U. Habermeier, B. Keimer, H. N. Lee, *Phys. Rev. B Condens. Matter Mater. Phys.* **2010**, *82*, 201407.

© 2024 The Author(s). Advanced Electronic Materials published by Wiley-VCH GmbH

2199160x, 2025, 2, Downloaded from https://advanced.onlinelibrary.wiley.com/doi/10.1002/aelm.202400565 by Forschungszentrum Jülich GmbH Research Center, Wiley Online Library on [21/02/2025]. See the Terms and Conditions (https://onlinelibrary.wiley.com/terms-and-conditions) on Wiley Online Library for rules of use; OA articles are governed by the applicable Creative Commons License